



Exploring the Limits of the Rapid-Charging Performance of Graphite as the Anode in Lithium-Ion Batteries

Wei Xu,¹ Connor Welty,¹ Margaret R. Peterson,¹ Jeffrey A. Read,² and Nicholas P. Stadie^{1,*} 

¹Department of Chemistry & Biochemistry, Montana State University, Bozeman, Montana 59717, United States of America

²Battery Science Branch, Sensors and Electron Devices Directorate, Army Research Laboratory, Adelphi, Maryland 20783, United States of America

Graphite is, in principle, applicable as a high-power anode in lithium-ion batteries (LIBs) given its high intralayer lithium diffusivity at room temperature. However, such cells are known to exhibit poor capacity retention and/or undergo irreversible side reactions including lithium plating when charged at current rates above $\sim 2\text{ C}$ ($\sim 740\text{ mA g}^{-1}$). To explore the inherent materials properties that limit graphite anodes in rapid-charge applications, a series of full-cells consisting of graphite as the anode and a standard $\text{Li}[\text{Ni}_{0.8}\text{Mn}_{0.1}\text{Co}_{0.1}]\text{O}_2$ (NMC811) cathode was investigated. Instead of a conventional cathode-limited cell design, an anode-limited approach was used in this work to ensure that the overall cell capacity is only determined by the graphite electrode of interest. The optimized N:P capacity ratio was determined as N/P = 0.67, enabling stable cycling across a wide range of charging rates (4–20 C) without inhibition by the NMC811 cathode. The results show that unmodified, highly crystalline graphite can be an excellent anode for rapid-charge applications at up to 8 C, even with a standard electrolyte and NMC811 cathode and in cells with 1.0 mAh cm^{-2} loadings. As a rule, capacity and specific energy are inversely proportional to crystallite size at high rates; performance can likely be improved by electrolyte/cathode tuning.

© 2022 The Author(s). Published on behalf of The Electrochemical Society by IOP Publishing Limited. This is an open access article distributed under the terms of the Creative Commons Attribution Non-Commercial No Derivatives 4.0 License (CC BY-NC-ND, <http://creativecommons.org/licenses/by-nc-nd/4.0/>), which permits non-commercial reuse, distribution, and reproduction in any medium, provided the original work is not changed in any way and is properly cited. For permission for commercial reuse, please email: permissions@iopublishing.org. [DOI: [10.1149/1945-7111/ac4b87](https://doi.org/10.1149/1945-7111/ac4b87)]



Manuscript submitted November 17, 2021; revised manuscript received December 28, 2021. Published January 24, 2022. *This paper 1836, was presented during the 240th Meeting of the Electrochemical Society, October 10–14, 2021.*

Supplementary material for this article is available [online](#)

Graphite has remained the workhorse anode in lithium-ion batteries (LIBs) since it was first commercialized by Sony in the 1990s,^{1,2} mainly due to its appreciable capacity (372 mAh g^{-1} as LiC_6), low operating potential ($\sim 0.1\text{ V}$ vs Li/Li^+), low overpotential (as low as 0.03 V), relatively low cost ($\sim 13\text{ USD kg}^{-1}$), and admirable safety (especially compared to metallic Li).^{3–5} However, graphite anode-based LIBs are often considered as unsuitable for rapid charging (defined herein as $\geq 4\text{ C}$, or $\geq 1.5\text{ A g}^{-1}$), limiting their application in certain extreme applications and slowing their widespread adoption over other energy storage chemistries in conventional everyday use.^{6,7} Significant capacity loss at a rate of 2 C or higher (for graphite anodes without any coating or other specific processing) is generally observed.^{8–11} While the diffusivity of Li^+ varies widely within a typical graphite-based LIB (between 10^{-12} to $10^{-6}\text{ cm}^2\text{ s}^{-1}$), the intralayer solid-state diffusivity of graphite is at the higher end of this range: 10^{-7} – $10^{-6}\text{ cm}^2\text{ s}^{-1}$ at room temperature.^{12–14} The rate-limiting step for lithium diffusion from the cathode to the anode is typically accepted to be the desolvation of Li^+ out of solution in the liquid electrolyte at the anode interface.¹⁵ Several correlated effects occurring at the anode surface contribute to slow lithiation of the graphite including concentration polarization and/or premature lithium plating.¹⁶ Hence, while the precise reasons for the slow charging (i.e., lithiation rate of graphite) remain incompletely understood, the sluggish desolvation kinetics of Li^+ at the graphite-electrolyte interface is often considered a crucial component of the overall explanation.

Numerous efforts have been made to investigate the role of the energy barrier of Li^+ desolvation at the SEI/electrolyte interface as a limiting factor for the high-rate performance of LIBs.^{17–19} Most recent studies have focused on the surface modification or amorphous coating of the graphite anode to facilitate desolvation and reduce the concentration polarization effect.^{6,20–23} However, rather than modifying or replacing graphite as the active anode material in

LIBs, we seek to understand the ultimate limits inhibiting its use in rapid-charge applications. Specifically, we explore herein the effects of its crystallinity and natural particle size and morphology on reversible capacity, at current rates up to 20 C (7.4 A g^{-1}). In this work, a series of full-cell LIBs consisting of one of five different types of graphite as the anode, a standard commercially available transition metal oxide as the cathode, and a common “Gen2” LiPF_6 electrolyte were investigated. In contrast to the conventional LIB design where the anode is in excess capacity compared to the cathode, in this study a cathode-rich model was chosen to ensure that the full-cell capacity was only determined by the performance of the graphite anode. The capacity ratio of the negative to positive electrode (N:P ratio) was optimized specifically for this study, permitting the characterization of the effects of numerous materials properties on electrochemical performance. Lastly, the effects of loading thickness were also explored, permitting the future engineering of optimized graphite-based cells for larger-scale rapid-charging applications.

Experimental

Materials.—Four commercial artificial graphite (AG) powders and one natural graphite (NG) powder were obtained for inter-comparison in this work, referred to as follows: AG-100 (SP-1 grade graphite, nominal particle size: $100\text{ }\mu\text{m}$, Bay Carbon Inc.), AG-50 (synthetic graphite, Timrex SLP50, nominal particle size: $50\text{ }\mu\text{m}$, Timal Ltd), AG-20 (synthetic graphite 282863, nominal particle size: $<20\text{ }\mu\text{m}$, Sigma-Aldrich), AG-1 (synthetic graphite “28,286-3,” nominal particle size: $1\text{--}2\text{ }\mu\text{m}$, Aldrich), and NG-1 (natural graphite, nominal particle size: $0.4\text{--}1.2\text{ }\mu\text{m}$, U.S. Research Nanomaterials Inc.).

The following materials were used in the preparation of electrochemical cells: lithium hexafluorophosphate (LiPF_6 , battery grade, Gotion Inc.), ethylene carbonate (EC, battery grade, Gotion Inc.), ethylmethyl carbonate (EMC, battery grade, Gotion Inc.), fluoroethylene carbonate (FEC, battery grade, Gotion Inc.), $\text{LiNi}_{0.8}\text{Mn}_{0.1}\text{Co}_{0.1}\text{O}_2$ (NMC811, battery grade, D₅₀: $9\text{--}15\text{ }\mu\text{m}$, MTI Corp.), lithium metal (chips, 99.9%, MTI Corp.), glass microfiber

*Electrochemical Society Member.

^zE-mail: nstadie@montana.edu

discs (0.67×257 mm, GF/D grade, catalogue number 1823–257, Whatman), carbon black (Super P, Timcal Ltd), polyvinylidene fluoride (PVDF, 99.5%, MTI Corp.), N-methyl-2-pyrrolidone (NMP, 99.0%, Sigma-Aldrich), copper foil (thickness: $9 \mu\text{m}$, MTI Corp.), and aluminum foil (thickness: $15 \mu\text{m}$, MTI Corp.).

Materials characterization.—Powder X-ray diffraction (XRD) measurements were performed on a Bruker D8 Advance diffractometer using $\text{Cu K}\alpha_{1,2}$ radiation ($\lambda = 0.15406$ nm) in Bragg-Brentano geometry. Nitrogen adsorption/desorption isotherms were measured at 77 K between 10^{-4} and 100 kPa using an automated volumetric instrument (3Flex, Micromeritics Instrument Corp.). Specific surface areas were calculated by the Brunauer–Emmett–Teller (BET) method between $P/P_0 = 0.008$ – 0.12 , and micropore volumes were calculated by the Dubinin–Radushkevich (DR) method.²⁴ Scanning electron microscopy (SEM) was performed using a Zeiss SUPRA 55VP microscope, operated at 20 kV. Samples were prepared for SEM by spreading a small quantity of powder on the surface of conductive carbon tape. Optical imaging was performed using a flow-through particle analyzer (FS5, Valmet Oyj); 25 mg of each sample was dispersed in 500 ml of water. Particle size analysis was performed by measuring ~ 100 s of representative particles (SEM) or ~ 10000 s of representative particles (optical images) using the ImageJ software package (v 1.51w). Raman spectroscopy was performed on a LabRAM HR Evolution spectrometer (Horiba Scientific Ltd) equipped with a confocal microscope using a 532 nm excitation source with an incident power of 10 mW.

Electrode fabrication.—Graphite anodes were prepared by mixing one of the graphite powders (80 wt%) with carbon black (10 wt%) and PVDF as the binder (10 wt%), and then forming a slurry in NMP (e.g., $\sim 300 \mu\text{l}$ per 200 mg batch). After grinding by hand for 20 min, the slurry was cast onto Cu foil using a doctor blade, air-dried at 80°C for 12 h, and then transferred to a 100°C vacuum oven to further remove moisture and residual solvent for an additional 12 h. Homogeneous loadings (0.5 – 1.2 mAh cm^{-2}) were achieved to within 0.05 mg cm^{-2} (0.02 mAh cm^{-2}). The graphite electrodes were cut into disks with a diameter of 10 mm, and then stored in an Ar-filled glovebox (<0.1 ppm $\text{H}_2\text{O}/\text{O}_2$) until further use.

NMC811 cathodes were prepared by mixing NMC811 powder (80 wt% of the final cathode) together with carbon black (10 wt%) and PVDF as the binder (10 wt%). First, the NMC811 and carbon black were ball-milled at 200 rpm in four cycles for 120 min total, with a 10 min rest period between each 30 min milling cycle. This mixture was then added to PVDF and a slurry was prepared by adding NMP (e.g., $\sim 50 \mu\text{l}$ per 100 mg batch). The resultant slurry was cast onto Al foil using a doctor blade, air-dried at 80°C for 12 h, and then transferred to a 100°C vacuum oven to further remove moisture and residual solvent for an additional 12 h. Homogeneous loadings were achieved to within 0.2 mg cm^{-2} . The NMC811 electrodes were cut into disks with a diameter of 12.7 mm, and then stored in an Ar-filled glovebox (<0.1 ppm $\text{H}_2\text{O}/\text{O}_2$) until further use.

Standard NMC811 cathodes (A-C020A, SNMC03004, lot 12846, 1.50 mAh cm^{-2}) were also obtained from the U.S. Department of Energy (DOE) Cell Analysis, Modeling, and Prototyping (CAMP) facility at Argonne National Laboratory (ANL) and used as received.

Electrochemical cell fabrication.—Stainless steel coin cells (316 SS, size 2032, Xiamen AOT Electronics Technology Co.) were assembled in an Ar-filled glovebox using graphite as the anode, NMC811 as the cathode, a glass microfiber disc as the separator (16 mm diameter), 1.2 M LiPF_6 in EC/EMC (3:7 mass ratio) with 2 wt% FEC as the electrolyte ($125 \mu\text{l}$), and a conical spring and 1.0 mm thick spacer. Custom three-electrode fluoropolymer cells were also assembled using lithium metal as the reference electrode,

as described in the Supporting Information (Fig. S1 (available online at stacks.iop.org/JES/169/010531/mmedia)).

Electrochemical measurements.—Galvanostatic charge and discharge cycling was performed in a temperature-controlled incubator (KB 53, Binder GmbH) at 25.0°C using a battery cycler (CT30001A, Landt Instruments). All cells underwent a conditioning protocol comprising a formatting cycle at 0.1 C and then five formation cycles at 0.2 C to establish a stable initial capacity. Additional cycles were then carried out at higher current rate(s) (e.g., 4 C, 6 C, 8 C, 10 C, and 20 C) to evaluate rapid-charging performance and rate capability. The charge step was performed using a constant current constant voltage (CCCV) protocol wherein a constant current was first applied (according to an idealized capacity of 370 mAh g^{-1}) until the cutoff voltage was reached, and then the voltage was held constant until the total charging time limit was reached (as determined by the desired practical C rate). For example, during a CCCV charge step at 10 C, the cell was first charged at 3.70 A g^{-1} until the cutoff voltage was reached (e.g., typically taking 2 min), and then further charged at the cutoff voltage for the remaining time expected in a 10 C charge (e.g., typically an additional 4 min). The discharge step was always performed using a constant current (CC) protocol; for N:P ratio optimization, the discharge rate was 4 C (1.48 A g^{-1}), according to an idealized capacity of 370 mAh g^{-1} and for all other tests, the discharge rate was 1 C (370 mA g^{-1}). In rate capability experiments, three rest cycles at 0.2 C were carried out between each set of 20 rapid charge cycles to monitor the health of the cell. Electrochemical impedance spectroscopy (EIS) was measured using a single-channel potentiostat (VersaSTAT 4–450, Princeton Applied Research) in the frequency range of 100 kHz to 10 mHz at open circuit voltage with an amplitude of 5 mV.

Electrochemical calculations.—Reversible discharge capacity was measured and normalized per active mass of graphite in each full-cell. The reversible capacity is related to the specific energy based on the average discharge voltage as follows:

$$E = Q \cdot V_{\text{avg}}$$

where E is the specific energy (per mass of graphite), Q is the reversible discharge capacity (per mass of graphite), and V_{avg} is the average voltage along the discharge profile. Specific power relevant to rapid charging can then be calculated as follows:

$$P = \frac{E}{t}$$

where P is the specific (charge) power, E is the specific (discharge) energy, and t is the total time taken to charge (e.g., 10 min at 6 C).

To convert the above electrode-specific quantities into insightful estimates of a commercial-scale full-cell (as opposed to a laboratory-scale coin cell), a modelling tool developed by researchers at ANL (BatPaC, v. 4.0) was employed to determine the total mass of a full-cell based on the required mass of graphite, NMC811, binder, and conductive additive necessary to assemble a large-scale, anode-limited graphite/NMC811 full-cell configuration as explored herein. Two scaling factors were used to convert graphite-specific to full-cell-specific energy and power: 0.2616 for plug-in hybrid electric vehicle (PHEV) batteries and 0.3320 for micro-hybrid electric vehicle (m-HEV) batteries, as a lower and upper bound on commercial-scale cells, respectively. An example calculation is provided in the Supporting Information (Section S9).

Note: all current rates in this work are based on the idealized capacity of graphite as 370 mAh g^{-1} . All areal loadings were calculated based on the practical capacity of graphite as 350 mAh g^{-1} and the practical capacity of NMC811 as 180 mAh g^{-1} .

Results and Discussion

Characterization of graphite powders.—Five commercially available graphite powders with a diversity of textural and morphological properties were first examined by scanning electron microscopy (SEM) to characterize particle shape and size. All five powders demonstrated flake-like morphology rather than a more spherical shape, as shown in Fig. 1. Upon particle size analysis, the average SEM diameter was found to be smaller than the corresponding nominal size (indicating a pass-through mesh separation), except for the nominally 1–2 μm artificial graphite (AG-1) whose actual size is $9.6 \pm 2.0 \mu\text{m}$ (see Table I). It is notable that the $\sim 1 \mu\text{m}$ natural graphite (NG-1) displays a much lower aspect ratio (diameter/thickness = 2.3) than the other graphites (diameter/thickness = ~ 20), which could indicate a different relative contribution from surface area at graphitic edge sites. Higher magnification imaging

indicates that the larger particle graphites (AG-50 and AG-100) exhibit clear flake boundaries and excellent crystallinity, while the smaller-sized graphites (AG-20, AG-1, and NG-1) display disordered edges and particle agglomeration. Nitrogen adsorption measurements also corroborate this observation of a distinct change in particle structure between AG-20 and AG-50 (Fig. S2 and Table SI).

The crystalline structure of each graphite was characterized by powder X-ray diffraction (XRD), to assess the stacking order and average crystallite size. The resulting XRD patterns including two high-resolution regions of interest are shown in Figs. 2a–2c. All five graphites exhibit an intense (002) reflection and relatively weak (004) reflection at 26.5° and 54.7° , respectively. The (100) and (101) reflections, centered at 42.4° and 44.6° , respectively, are barely observed in the larger-sized graphites (AG-50 and AG-100) since orientation is highly preferred along (00 \bar{l}). The smaller-sized

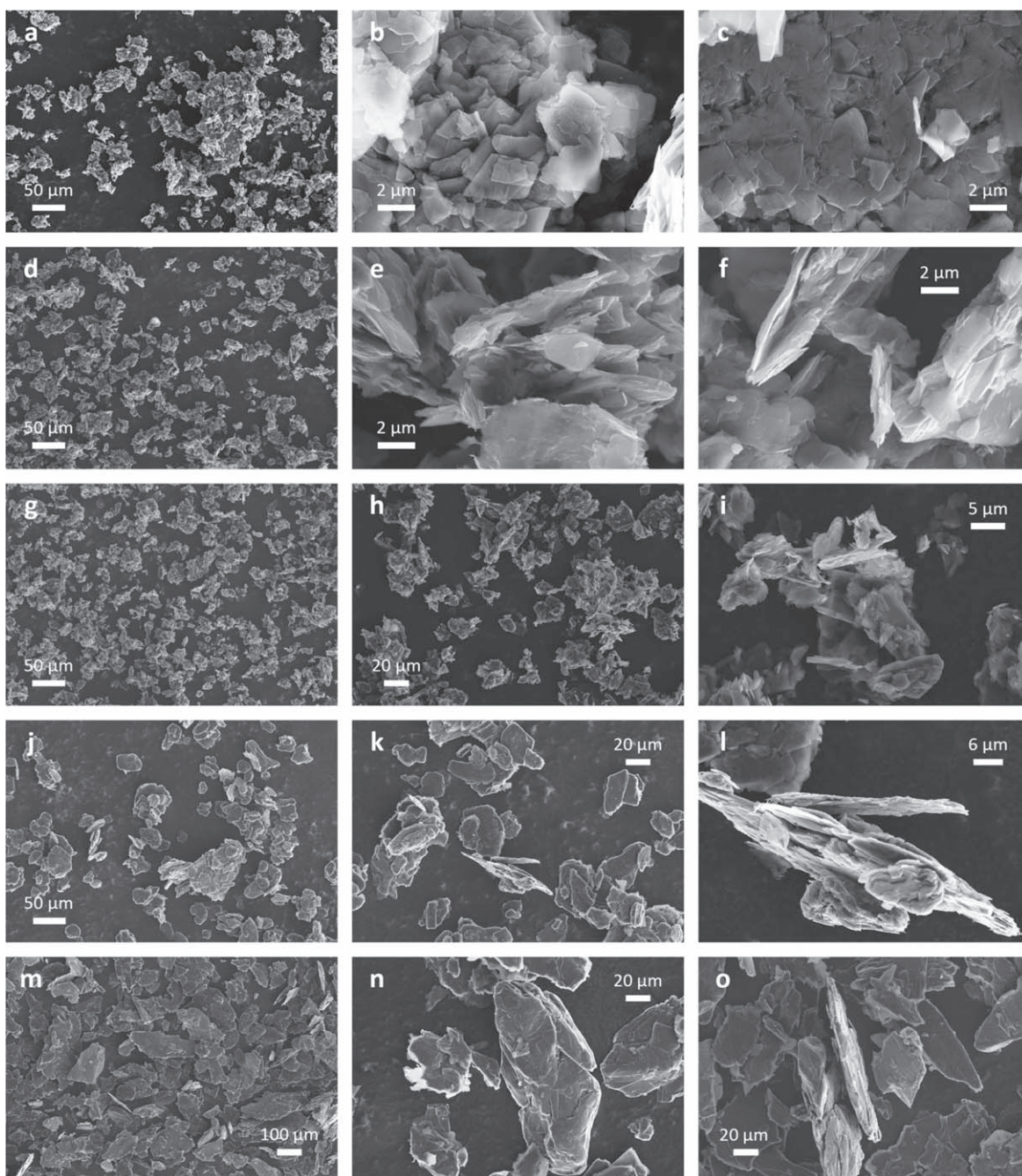


Figure 1. SEM micrographs of five commercial graphite powders with nominal particle size from 1–100 μm : (a)–(c) NG-1, (d)–(f) AG-1, (g)–(i) AG-20, (j)–(l) AG-50, and (m)–(o) AG-100.

Table I. Materials properties of five commercially available graphite powders.

Graphite	Nominal particle size (μm)	Particle size ^{a)} (μm)	Aspect ratio ^{a)}	Crystallite size ^{b)} (nm)	Interlayer spacing ^{b)} (\AA)	G peak FWHM ^{c)} (cm^{-1})
NG-1	0.4–1.2	0.73 ± 0.2	2.3	49.8	3.36	26.3
AG-1	1	9.6 ± 2.0	21.3	47.6	3.36	32.9
AG-20	20	15.2 ± 3.5	20.0	41.5	3.37	34.4
AG-50	50	20.5 ± 5.5	17.1	97.7	3.35	28.2
AG-100	100	74.5 ± 22.0	18.6	96.7	3.35	25.9

a) Measured by SEM analysis, arithmetic mean. b) Measured by XRD analysis of the (002) reflection. c) Measured by Raman analysis of the G peak at 1570–1580 cm^{-1} .

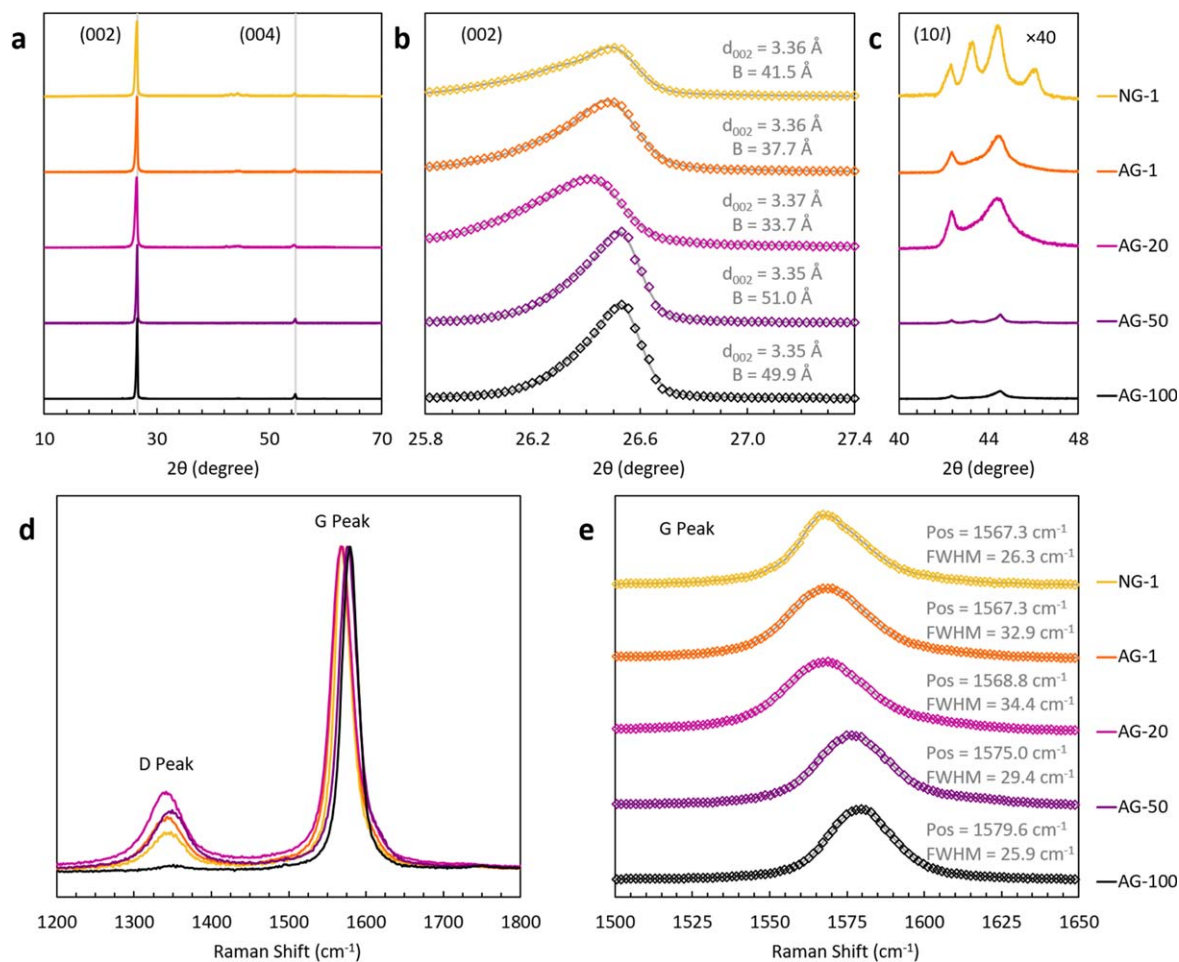


Figure 2. Structure and crystallinity of five commercial graphite powders with nominal particle size from 1–100 μm : (a) XRD patterns with an emphasis on (b) the (002) reflection and (c) the (10l) family of reflections, and (d) Raman spectra with an emphasis on (e) the G peak as an indicator of in-plane ordering.

artificial graphites (AG-20 and AG-1) exhibit a broad (10l) family of reflections owing to a reduced orientation preference. These results in terms of the degree of (00l) orientation preference are in excellent agreement with the SEM results, but it is unclear whether this preference is still retained upon electrode preparation. Scherrer analysis of crystallite size was carried out using the (002) reflection, indicating a very different ranking of the graphites than that indicated by particle size: 96.7 nm for AG-100, 97.7 nm for AG-50, 41.5 nm for AG-20, 47.6 nm for AG-1, and 49.8 nm for NG-1, as shown in Table I. The position of the (002) reflection (indicating the graphite interlayer spacing) is slightly different among the samples, but not significantly above experimental error. Lastly, it is notable that NG-1 exhibits a very different (10l) family of reflections that is more consistent with an ABC-stacked graphitic lattice commonly found in nanocrystalline graphites (see Fig. S3).

Raman spectroscopy was used to investigate the in-plane crystallinity of each graphite sample; spectra collected at an incident wavelength of 532 nm are shown in Figs. 2d–2e. Each sample is characterized by an intense G peak at 1567–1580 cm^{-1} and a minor to insignificant D peak at $\sim 1350 \text{ cm}^{-1}$, indicating that all samples lie within the crystalline to amorphous sp^2 -hybridized carbon regimes (stages 1–2) of Ferrari’s amorphization trajectory.²⁵ Owing to the complex (non-monotonic) dependence of such properties as G peak position and the $I_D:I_G$ ratio on crystallinity, the full-width half-maximum (FWHM) of the G peak is used herein as a direct indicator of in-plane graphitic ordering, as shown in Table I. The largest flake graphites with large Scherrer crystallite size (AG-50 and AG-100) exhibit the narrowest G peak FWHM, indicating high overall crystallinity. The intermediate sized graphites (AG-1 and AG-20)

with the smallest Scherrer crystallite size exhibit the broadest G peak FWHM, indicating poorer in-plane ordering. Interestingly, NG-1 seems to exhibit relatively high in-plane ordering (narrow G peak FWHM) despite its modest *c*-axis ordering (i.e., Scherrer (002) crystallite size), though its peak shape is different and it remains an outlier among the graphites explored in this work. The shape of the 2D peak confirms the ranking of in-plane crystallinity by G peak FWHM (Fig. S4).

Voltage cutoff determination in anode-limited full cells.—The Li/graphite half-cell is well-known to be disqualified as an acceptable means to accurately characterize the rapid-charging capability of graphite as the anode in full-cell LIBs due to the significant voltage polarization brought upon by the metallic Li counter electrode.^{8,26} The overpotential has been measured to be as large as 0.2 V in such half-cell configurations at 4 C, bypassing the stage-1 ($\sim 0.09 \text{ V vs Li/Li}^+$) and stage-2 ($\sim 0.12 \text{ V vs Li/Li}^+$) lithiation/delithiation processes, resulting in much lower capacity retention than in comparable full-cell or three-electrode cell configurations. Hence, full-cell LIBs consisting of graphite as the anode coupled with NMC811 as the cathode were investigated herein. NMC811 was selected as an appropriate cathode for this study owing to its wide commercial availability, low cost, and acceptable charging (delithiation) kinetics.^{27,28}

Cell balance, or the ratio of anode to cathode capacity (N:P ratio), is a fundamental property warranting consideration in the realization of rapid-charging and stable long-term cycling of full-cell LIBs. In practical (commercial) LIBs, the anode is typically provided in excess owing to its low relative cost and, for safety reasons, to

prevent Li plating; the N:P ratio is typically set between $N/P = 1.1$ – 1.2 . Higher N:P ratios can cause over-delithiation of the cathode, leading to irreversible decomposition in some cases (e.g., as in NMC-type cathodes²⁸) and/or electrolyte oxidation, inhibiting long-term cycling stability. In general, N:P ratios far from $N/P = 1$ decrease the overall energy density of the full-cell on account of the unused active mass of the electrode in excess; this issue is exacerbated under rapid-charging conditions where the electrode capacity is not fully utilized. In contrast to previous studies, these issues are addressed in the present work by adopting a cathode-rich cell design to ensure that the graphite anode always imposed the overall limitation on full-cell capacity.

The issues pertaining to cell balance are schematically depicted in Fig. 3. An idealized, balanced graphite/NMC811 cell ($N/P = 1$) could in principle be charged at very low rates to the target cutoff voltage, leading to the measurement of its true, full-cell capacity (Fig. 3a). However, at rapid charging rates (Fig. 3b), this scenario is not realistic; capacity loss due to kinetic limitations is inherently different at each electrode. In graphite/NMC811 full-cells, this loss is typically greater at the cathode.^{29,30} Therefore, the idealized N:P ratio (based on the low-rate cycling of a new full-cell) must be altered to ensure a graphite-limited cell capacity by increasing the cathode loading. Reducing the N:P ratio, for example to $N/P = 0.67$, ensures a graphite-limited full-cell capacity at both low and high rates. However, when altering the N:P ratio while still applying the same target cutoff voltage as for a balanced cell, graphite over-charging will be observed and its potential will drop to at or below 0 V vs Li/Li^+ , significantly increasing the risk for Li plating. By enacting an appropriate full-cell cutoff voltage (e.g., 4.0 V for $N/P = 0.67$ at low rates, Fig. 3a), it is possible to ensure that the graphite anode is maintained at its target minimum potential of 0.05 V vs Li/Li^+ , thereby preventing Li plating while still achieving a fundamentally anode-limited full cell.

The first cycle charging profiles of graphite (AG-20) and NMC811 in a three-electrode cell designed to mimic a full-cell with $N/P = 0.61$ are shown in Fig. 3c; the onset of Li plating is observed at $\sim 495 \text{ mAh g}^{-1}$ (normalized to the active mass of graphite). Importantly, when the graphite potential reaches 0.01 V vs Li/Li^+ , the full-cell voltage is only 3.73 V, significantly lower than the typical 4.2 V cutoff voltage expected for a conventional LIB full-cell with $N/P > 1$. Thus, the onset capacity of Li plating in the first charging cycles was applied herein as a critical indicator to determine the cutoff voltage for the subsequent charging cycles. The first cycle charge capacity limit (i.e., the onset of Li plating) occurs at 490–500 mAh g^{-1} for all five different graphites explored herein, and is independent of the N:P ratio (Fig. S5). To absolutely ensure the prevention of Li plating, 475 mAh g^{-1} was selected as the capacity limit, and the voltage reached at 475 mAh g^{-1} was applied as the cutoff voltage during the charging process for all full-cells in this work.

Extremely cathode-rich cell designs based on NMC811 as the cathode cause the counter-intuitive issue of over-lithiation of the cathode upon discharge, leading to a far lower full-cell discharge voltage and therefore a misleading analysis of the state of discharge of the graphite anode. This is demonstrated by the galvanostatic charge/discharge profiles of graphite and NMC811 in a three-electrode cell configuration designed to mimic a full-cell with $N/P = 0.25$, as shown in Fig. 3d. The charging process in this configuration follows a similar profile as for less cathode-rich configurations, and the onset of Li plating is prevented by controlling the graphite potential to 0.01 V vs Li/Li^+ , corresponding to a full-cell voltage of 3.65 V. However, upon subsequent 4 C discharge of the graphite to a potential of 1.5 V vs Li/Li^+ , the NMC811 cathode transitions to a second plateau at a potential of $\sim 1.8 \text{ V}$ vs Li/Li^+ and the full-cell voltage is reduced to only 0.3 V at the end of discharge. The second discharge plateau for NMC811 corresponds to

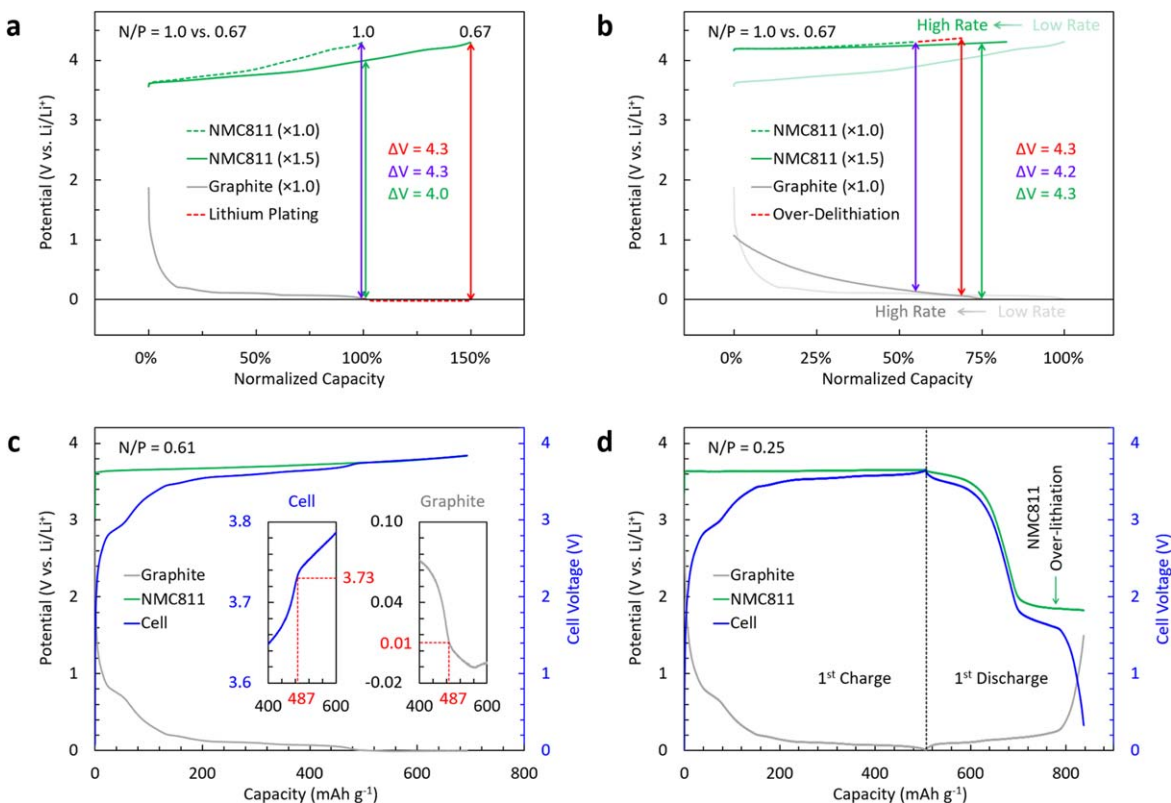


Figure 3. Schematic and experimental description of charge/discharge cycling cutoff in anode-limited graphite/NMC811 full-cells. (a)–(b) Schematic voltage profiles of graphite (gray), NMC811 (green), and the difference (ΔV , red, yellow, and green) at two simulated N:P capacity ratios ($N/P = 1.0$ and 0.67), under (a) standard- and (b) rapid-charging conditions. The capacity in (a)–(b) is normalized to that of the slow-rate graphite anode. (c) Experimental first charge voltage profiles of graphite and NMC811 with an N:P ratio of 0.61, and (d) experimental first cycle voltage profiles of graphite and NMC811 with an N:P ratio of 0.25. The specific capacities in (c)–(d) were calculated based on the active mass of the graphite anode and the experimental current rate was 0.1C (37 mA g^{-1}).

the over-lithiation of a surface layer within the cathode, typically brought upon by the slow diffusion rate of lithium within the crystal structure of highly lithiated $\text{Li}_x\text{Ni}_y\text{Mn}_z\text{Co}_{1-y-z}\text{O}_2$ compositions. The plateau observed herein at ~ 1.8 V vs Li/Li^+ is consistent with the over-lithiation plateau observed at ~ 1.65 V vs Li/Li^+ for $\text{Li}_x\text{Ni}_{0.6}\text{Mn}_{0.2}\text{Co}_{0.2}\text{O}_2$ between $x = 1.0$ – 1.4 in previous work.³¹ It was further revealed in previous work that the oxidation state of all three transition metals in the NMC cathode remain approximately the same in the over-lithiated electrode, but only up to an over-lithiation of 20% after which a new lithiation plateau at even lower potential is eventually observed (e.g., at ~ 0.8 V vs Li/Li^+ for NMC622), corresponding to a significant reduction of all three transition metals. To balance the ability to resolve the optimal performance of graphite and the degree of over-lithiation of the NMC811 cathode, in the present study the full-cell voltage was limited to 1.0 V during discharge. At this cutoff voltage, an adequate reversible capacity of ~ 350 mAh g^{-1} could be realized at the graphite anode, and meanwhile the degree of over-lithiation of the cathode was controlled to below 20%.

N:P ratio optimization.—An anode-limited cell design, as discussed above, is used herein to assess the ultimate rate capability of unmodified graphite in the presence of NMC811 and a standard Gen2 electrolyte. However, it is not possible (a-priori) to know the optimal N:P ratio of a full-cell under rapid charging conditions since it depends sensitively on both the formation of SEI (which consumes Li and therefore diminishes the true reversible capacity of the cathode) and the degree of capacity loss in the anode (the subject of this study). This design is akin to a pre-lithiation strategy³² except that it does not rely on any modification of the electrode materials or any pre-treatment of the anode; the effects of pre-lithiation on full-cell energy density have been recently reported elsewhere.³³

In order to determine the optimal starting N:P ratio of cathode-rich graphite/NMC811 full-cells, a series of cells between N/P = 0.57–0.71 were prepared, based on the results of preliminary studies to narrow this range (Fig. S6). A standard NMC811 electrode with an areal capacity of 1.5 mAh cm^{-2} was used as-received from Argonne National Laboratory as the cathode. The graphite anode loading was then varied to achieve different N:P ratios, based on a reversible specific capacity of 350 mAh g^{-1} (as determined by half-cell characterization); AG-20 was used as the model representative graphite for N:P ratio optimization studies. The six full-cell configurations of varying N:P ratio investigated herein are shown in Table II, corresponding to 41%, 45%, 50%, 55%, 63%, and 76% excess capacity in the cathode, respectively.

A comparison of the electrochemical performance of the graphite/NMC811 full-cells with varying N:P ratio is shown in Fig. 4. After a formatting cycle at 0.1 C, five additional formation cycles at 0.2 C were carried out to ensure the formation of a robust SEI, followed by 500 cycles of galvanostatic charge/discharge using a CCCV/CC protocol (where 1 C = 370 mA g^{-1} , see Experimental Methods). Total charging times according to the stated C-rate were enforced (e.g., 4 C = 15 min) and discharge was performed to 1.0 V, followed by a 30 s rest before proceeding to the next cycle. The percentage capacity retention was calculated with respect to the average discharge capacity achieved during the first 20 cycles under

4 C CCCV/CC cycling. The specific capacity of all full-cells first increased and then rapidly decreased within the initial ~ 50 cycles of 4 C CCCV/CC cycling; in subsequent cycles, the cells underwent a gradual decay in capacity of 10%–20%. The increasing capacity in the initial cycles is most likely owed to electrode activation (i.e., electrolyte infiltration and electrode equilibration effects such as particle fragmentation or coarsening). Full-cells with N:P ratios of N/P = 1.00/1.50 = 0.67 showed the least fluctuation and the highest average discharge capacity, retaining > 90% capacity after 500 cycles (Fig. 4a). Therefore, the N:P ratio corresponding to N/P = 0.67 was selected for subsequent investigations of the role of graphite materials properties and loading thickness on rapid-charging performance between 4–20 C.

Materials properties effects on rapid-charging performance.—Particle size reduction of graphite is typically considered to be beneficial to rapid-charging on the basis of both a shorter transport length between the desolvation interface and the lithium binding site and also a higher surface-to-volume ratio, resulting in a lower Li^+ concentration polarization prior to desolvation and intercalation. It is clear that the accessibility of Li^+ to the interlayer galleries where they eventually reside is critical to the rapid-charging performance of a graphite anode, especially under extremely rapid-charging conditions (≥ 4 C). Nevertheless, the impact of materials properties such as particle size, particle aspect ratio, crystallite size, and interlayer spacing of the graphite electrode remain rarely explored in a systematic way, despite the existence of numerous previous reports on surface modifications including nanosizing, amorphous surface coatings, and disordered hard carbon as an alternative to graphite for rapid-charge applications.

To determine the role of four key materials properties on the rapid-charging performance of graphite, five different commercially-available graphite powders with diverse materials properties were explored in this work, as shown in Fig. 5. Electrochemical characterization was conducted within full-cells consisting of graphite as the anode, NMC811 as the cathode, and an EC/EMC-based electrolyte, with an optimized N:P ratio of N/P = 0.67. Full-cells were tested at increasingly higher current rates of 4 C, 6 C, 8 C, 10 C, and 20 C, employing a CCCV charging protocol followed by a 1 C CC discharging protocol to eliminate the impact of cathode lithiation rate on performance. Three 0.2 C charging cycles were inserted between each series of cycles at higher rates to assess the health of the cell; a 30 s break was taken between each cycle, and five replicate cells were used to characterize each different graphite powder (Figs. S7–S8).

All five different graphites display an obvious capacity decay with increasing current rate between 4–20 C, indicating greater and greater concentration polarization resulting from kinetic limitations on Li^+ diffusion, preventing the complete formation of stage-1 LiC_6 before the time cutoff imposed by CCCV charging. While the reversible capacity during rapid-charging cycles showed a systematic decay in all cells (Figs. 5a–5b), the reversible capacity during the recovery cycles at 0.2 C was found to return to within 6% of the average capacity measured during the first five cycles (as shown in Fig. 5a and Figs. S7–S8). Furthermore, no significant capacity decay was observed within each of the rapid-charging sets

Table II. Two-electrode coin cell configurations for N:P ratio optimization study.

Anode (N) ^{a)} (mAh cm^{-2})	Cathode (P) ^{b)} (mAh cm^{-2})	N:P ratio (N/P)	Cutoff voltage (V)
0.85	1.50	0.57	3.74
0.92	1.50	0.61	3.77
0.97	1.50	0.65	3.77
1.00	1.50	0.67	3.79
1.03	1.50	0.69	3.79
1.06	1.50	0.71	3.81

a) calculated based on a reversible specific capacity of 350 mAh g^{-1} . b) standard electrode from Argonne National Laboratory.

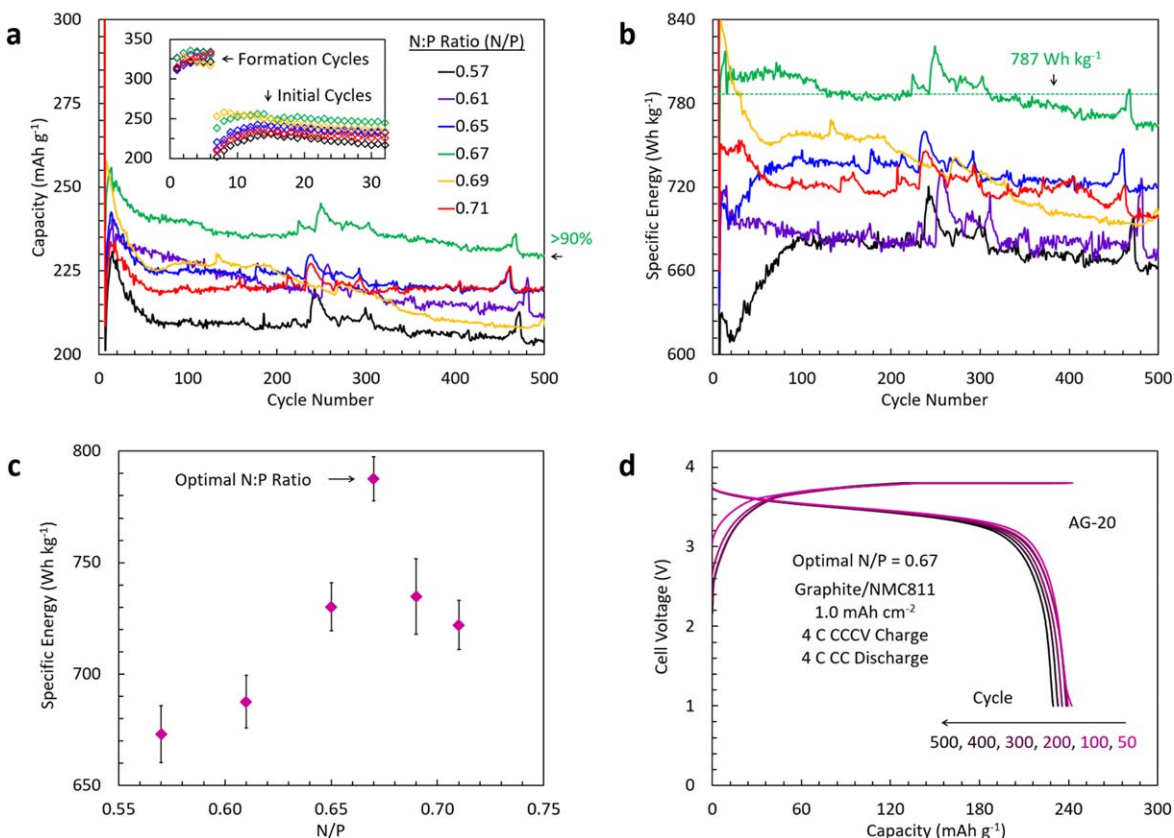


Figure 4. N:P ratio optimization of anode-limited graphite/NMC811 full-cells based on AG-20 as the anode: comparison of (a) discharged capacity (normalized per active mass of graphite), (b) discharged specific energy (normalized per active mass of graphite), (c) average discharged specific energy over 500 cycles as a function of N/P, and (d) galvanostatic charge/discharge voltage profiles for a representative full-cell with N/P = 0.67.

comprising 20 cycles at the same rate for any of the five graphites explored. Together, these findings suggest that the cathode-rich, anode-limited full-cell design with an optimized N:P ratio of N/P = 0.67 can be used to effectively assess the ultimate performance limitations on graphite under rapid-charging conditions.

Materials properties such as particle size and shape (controlling the surface area to volume ratio), crystallite size and shape (controlling the ratio of the number of crystalline edge sites to volume), and interlayer spacing (which may affect intralayer Li^+ diffusion) may all contribute to the differing reversible capacities of graphite under rapid-charging conditions. To shed insight on which of these properties plays the most significant role in the rapid-charging performance of graphite, a plot of reversible specific energy as a function of each parameter can be investigated; the two most significant trends are shown in Fig. 5d. While there is no systematic trend between reversible specific energy (or reversible capacity) and either particle size or particle shape (aspect ratio), there is a systematic increase in specific energy with increasing interlayer spacing and a concomitant decrease in specific energy with increasing crystallite size. The opposite trend appears at low rates (e.g., 0.2 C as shown in the lower right of Fig. 5c). The trend in interlayer spacing is weakly evidenced owing to very similar d_{002} -spacing. Hence, we conclude that crystallite size along the [002] stacking direction is the most reliable factor that determines the high rate electrochemical performance of graphite as an anode in LIBs. Within the series of graphite materials investigated herein, the sample with smallest crystallite size (AG-20) demonstrated the highest reversible capacity (241 mAh g^{-1}) and specific energy (809 Wh kg^{-1}), whereas the sample with the highest degree of crystallinity (AG-50) showed the lowest reversible capacity (226 mAh g^{-1}) and specific energy (678 Wh kg^{-1}). Experimental data as well as computational results have shown that Li^+ diffusion across

the electrode/electrolyte interface (10^{-10} – $10^{-12} \text{ cm}^2 \text{ s}^{-1}$) demonstrates the most sluggish kinetics along the entire path from cathode to anode upon charging, compared to diffusion within the liquid electrolyte (10^{-6} – $10^{-7} \text{ cm}^2 \text{ s}^{-1}$) and solid-state diffusion within the interlayer galleries of graphite (10^{-7} – $10^{-8} \text{ cm}^2 \text{ s}^{-1}$). Therefore, the Li^+ accessibility to the edge sites of the graphite crystallites (representing the precise location of the electrode/electrolyte interface) must be critical for the ability to rapidly lithiate the graphite anode.

Loading thickness effects on rapid-charging performance.—To explore the areal loading effects on the rapid-charging performance of graphite between 4–20 C, thin active material loadings from 0.5 to 1.2 mAh cm^{-2} were prepared, a requirement indicated by previous simulations of graphite/NCA full-cells.³⁴ In this work, full-cells were assembled with AG-20 as the anode and NMC811 as the cathode, fixing the N:P ratio at N/P = 0.67 for all loadings. The six additional full-cell configurations of varying areal loading are shown in Table III, corresponding to 0.50, 0.60, 0.70, 0.80, 1.10, and 1.20 mAh cm^{-2} at the anode. The discharge capacity and specific energy as a function of graphite anode loading under rapid-charging conditions (between 4–20 C) is shown in Figs. 6a–6b; the results at the standard loading of 1.0 mAh cm^{-2} from Fig. 5 are also shown for comparison. The graphite capacity diminishes with increasing loading due to reduced transport of Li^+ from the electrolyte to a binding site within the graphite structure, resulting in significant concentration polarization at the graphite interface.³⁵ Poor electrode utilization and increased local current densities in thicker loadings tend to induce the growth of metallic lithium dendrites; however, thinner loadings are generally considered to mitigate such polarization effects and reduce the probability of lithium plating under rapid charging conditions.^{36,37} In this work, full-cells with graphite areal

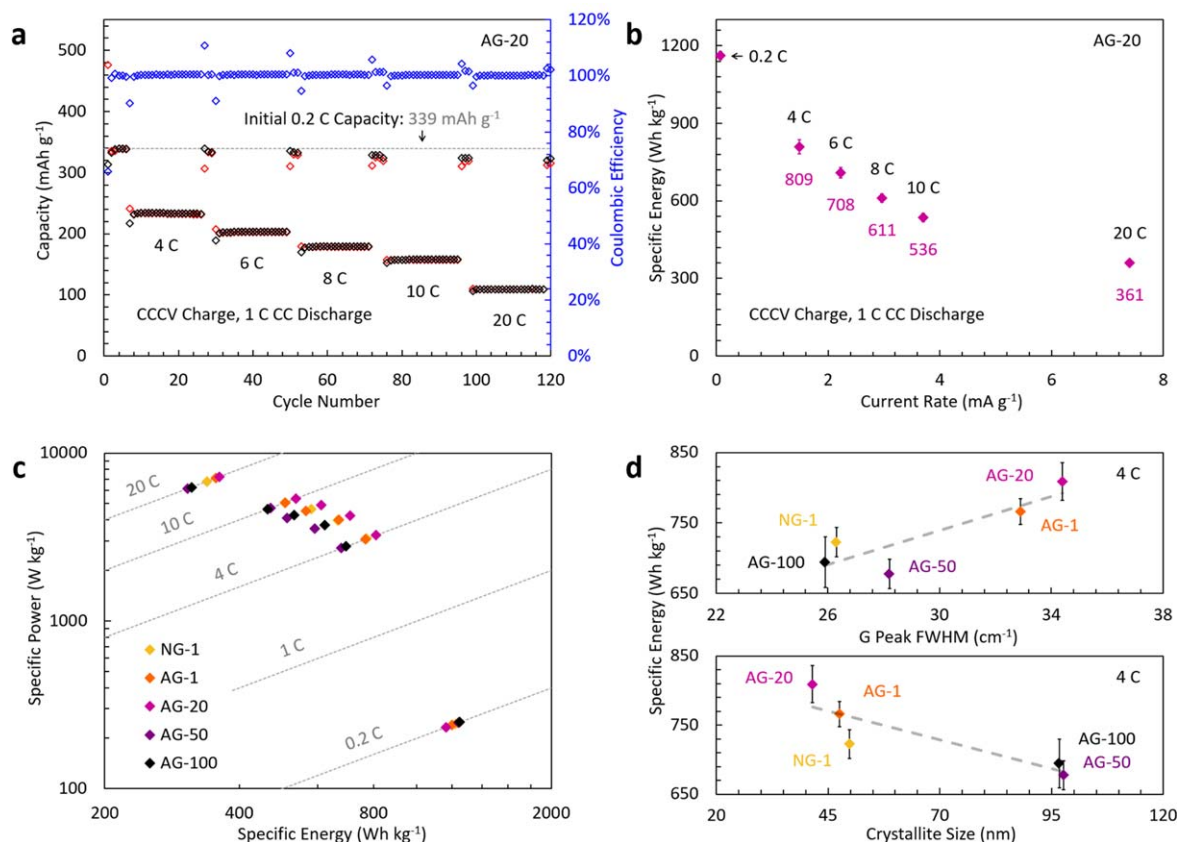


Figure 5. Rate capability and materials properties study of five commercial graphite powders with nominal particle size from 1–100 μm, using AG-20 as a representative example. (a) Charge/discharge capacity (red/black, respectively) and coulombic efficiency (blue) as a function of cycling for an AG-20/NMC811 full-cell with N/P = 0.67. (b) Reversible specific energy (20th cycle) as a function of current rate for AG-20 and (c) corresponding Ragone plot for all materials. (d) Reversible specific energy as a function of interlayer spacing (upper) and crystallite size (lower) for all materials.

Table III. Two-electrode coin cell configurations for electrode loading optimization study.

Anode (N) ^{a)} (mAh cm ⁻²)	Cathode (P) ^{b)} (mAh cm ⁻²)	N:P Ratio (N/P)
1.20	1.80	0.67
1.10	1.65	0.67
0.80	1.20	0.67
0.70	1.05	0.67
0.60	0.90	0.67
0.50	0.75	0.67

a) calculated based on a reversible specific capacity of 350 mAh g⁻¹. b) calculated based on a reversible specific capacity of 180 mAh g⁻¹.

loadings of 0.5 and 0.6 mAh cm⁻² were capable of charging at a rate of 8 C while still exhibiting >240 mAh g⁻¹ capacity or ~70% of the slow-rate capacity (350 mAh g⁻¹ at 0.2 C). In contrast, full-cells with a graphite areal loading of 1.2 mAh cm⁻² seem not appropriate for rapid-charging applications (4 C or higher); even at 4 C, electrodes with loadings of ≥ 1.2 mAh cm⁻² demonstrate a capacity corresponding to ≤50% of the slow-rate capacity.

Interestingly, areal loading effects are more significant at the 4 C current rate than at the extremely high 20 C rate explored in this study. The capacity difference between graphite anodes of 0.5 and 1.2 mAh cm⁻² loading upon cycling at 4 C was observed to be 105 mAh g⁻¹, whereas this capacity difference reduced to 75 mAh g⁻¹ upon cycling at 20 C. This observation indicates that capacitive adsorption dominates within the very short charging period under rapid charging at 20 C as opposed to the intercalation-based behavior at 4 C, and hence the concentration polarization is less dependent on the loading thickness of the electrode. This indicates that thinner loadings effect a more critical influence in most practically relevant

high rate applications (e.g., 4 C and 6 C) of graphite-based lithium-ion batteries.

In the cathode-rich full-cells with N/P = 0.67, current rates up to 20 C could be achieved without any detectable lithium plating, as determined by high-precision coulometry studies^{38–40} (see Figs. S9–S10). Voltage profiles of the representative full-cell comprising AG-20 as the anode (1.0 mAh cm⁻²) and NMC811 as the cathode (1.5 mAh cm⁻²) are shown in Fig. 6c. A Ragone plot that summarizes the performance of five replicate cells is shown in Fig. 6d, both graphite active material-specific (filled diamonds) and estimated full-cell-specific (magenta crosses) based on larger-scale cells designed for use in battery electric vehicles. The lower full-cell bound is based on cells designed for use in PHEVs while the upper bound is based on cells designed for use in micro-HEVs (see Experimental Methods). Comparable results for five replicate commercially-obtained 1 Ah cylindrical full-cells specifically tailored for rapid-charge applications (18500–1000TB, AA Portable Power Corp.) are also shown (turquoise crosses). The full-cells

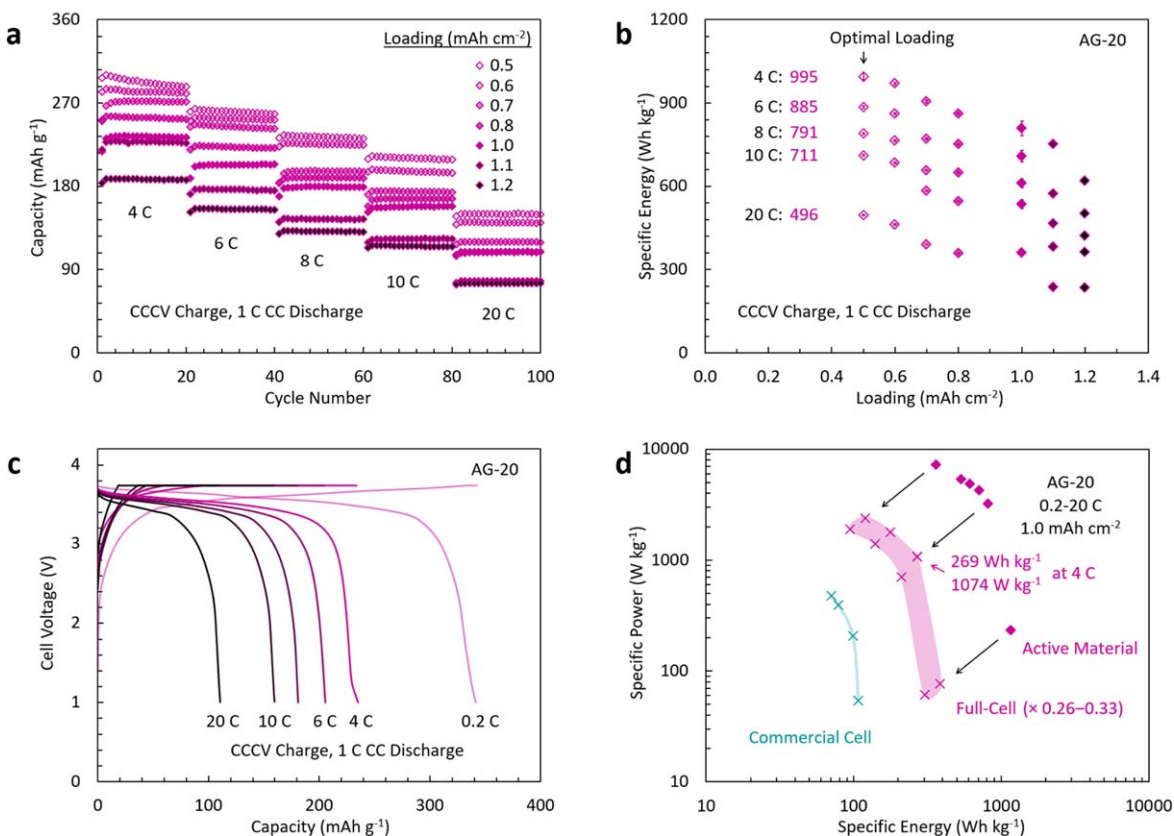


Figure 6. Optimization of electrode loading and summary of full-cell performance. (a) Discharge capacity as a function of areal loading (light to dark magenta) and current rate (as indicated), for AG-20/NMC811 full-cells while holding $N/P = 0.67$ constant. (b) Reversible specific energy (20th cycle) as a function of areal loading. (c) Charge/discharge voltage profiles for AG-20/NMC811 full-cells with an areal loading of 1.0 mAh cm^{-2} and (d) corresponding Ragone plot. The full-cell specific energy and power were calculated using a range of conversion factors (0.26–0.33) as implemented by the BatPaC modeling software. A commercial rapid-charge AA cylindrical cell is shown for comparison (turquoise).

developed in this work demonstrate a superior specific energy as well as specific power compared to the commercial cells, by a factor of 2.9–3.6 in energy and 2.3–2.8 in power, depending on the full-cell battery design (see Experimental Methods for details as to cathode-specific to cell-specific energy and power calculations). A specific energy of 269 Wh kg^{-1} can be achieved within a charge time of 15 min (corresponding to 1074 W kg^{-1}) based on the cathode-rich cell design implemented in the present work. Therefore, these results shown that by merely adopting an appropriate cell design and charging protocol, and not by modifying the anode material itself in any way, much higher rate capability than typically achieved for pure artificial graphite can be achieved.

Conclusions

While the reversible capacity of graphite does diminish as a function of increasing rate, graphite can still be an effective high-rate anode for LIBs in rapid-charge applications. In this work, cathode-rich cells with $N/P = 0.67$ could be cycled at current rates up to 20 C without any detectable lithium plating, and crystallite size was determined to be inversely proportional to electrochemical performance. Full-cells based on AG-20 as the anode demonstrate a superior specific energy as well as specific power compared to the commercial cells, by a factor of 3–4 in specific energy and a factor of 2–3 in power. The rate capability results indicate that graphite retains 240 mAh g^{-1} capacity at 4 C with a commercially viable 1.0 mAh cm^{-2} active mass loading; an even larger capacity of 285 mAh g^{-1} can be realized at a lower 0.5 mAh cm^{-2} loading. Hence, this study sheds new insights onto the limits of the rapid-charging capability of graphite as an anode in LIBs. Further cathode and/or electrolyte engineering can likely yield even better performance

without any modification of the graphite anode itself, lending significant credibility to pure, crystalline graphite as a rapid-charging anode for LIBs.

Acknowledgments

We thank Devin McGlamery for performing SEM, Sophia Randak for measuring Raman spectroscopy, and Dylan Cousins for particle size analysis based on optical imaging methods. We are grateful to ANL for providing the standard NMC811 cathodes and we also acknowledge MTI Corp. for partial support of equipment purchased within the MTI Sponsorship Program (MSP). Funding for this work was provided by the DEVCOM Army Research Laboratory (ARL) under cooperative agreement (W911NF-20-2-0284).

ORCID

Nicholas P. Stadie  <https://orcid.org/0000-0002-1139-7846>

References

1. M. Yoshino, R. J. Brodd, and A. Kozawa, *Lithium-Ion Batteries* (Springer, New York, NY) (2009).
2. A. Yoshino, *Angew. Chem. Int. Ed.*, **51**, 5798 (2012).
3. P. A. Nelson, A. Shabbir, K. G. Gallagher, and D. W. Dees, *Modeling the Performance and Cost of Lithium-Ion Batteries for Electric-Drive Vehicles* (2019), Argonne National Laboratory Technical Report ANL/CSE-19/2.
4. Y. P. Wu, C. Jiang, C. Wan, and R. Holze, *J. Power Sources*, **111**, 329 (2002).
5. C. von Lüdgers, V. Zinth, S. V. Erhard, P. J. Osswald, M. Hofmann, R. Gilles, and A. Jossen, *J. Power Sources*, **342**, 17 (2017).
6. D. S. Kim, Y. E. Kim, and H. Kim, *J. Power Sources*, **422**, 18 (2019).
7. J. C. Garcia, I. Bloom, C. Johnson, D. Dees, and H. Iddir, *J. Phys. Chem. C*, **124**, 8162 (2020).
8. S. S. Zhang, *J. Electrochem. Soc.*, **167**, 100510 (2020).

9. A. Laforgue, X.-Z. Yuan, A. Platt, S. Brueckner, F. Perrin-Sarazin, M. Toupin, J.-Y. Huot, and A. Mokrini, *J. Electrochem. Soc.*, **167**, 140521 (2020).
10. R. Dubey, M.-D. Zwahlen, Y. Shynkarenko, S. Yakunin, A. Fuerst, M. V. Kovalenko, and K. V. Kravchik, *Batteries Supercaps*, **4**, 464 (2021).
11. C. Mao, R. E. Ruther, J. Li, Z. Du, and I. Belharouak, *Electrochem. Commun.*, **97**, 37 (2018).
12. K. Persson, V. A. Sethuraman, L. J. Hardwick, Y. Hinuma, Y. S. Meng, A. van der Ven, V. Srinivasan, R. Kostecki, and G. Ceder, *J. Phys. Chem. Lett.*, **1**, 1176 (2010).
13. E. G. Leggesse, C.-L. Chen, and J.-C. Jiang, *Carbon*, **103**, 209 (2016).
14. J. H. Park, H. Yoon, Y. Cho, and C.-Y. Yoo, *Materials*, **14**, 4683 (2021).
15. K. Xu, *Chem. Rev.*, **104**, 4303 (2004).
16. K. Xu, *Chem. Rev.*, **114**, 11503 (2014).
17. T. R. Jow, S. A. Delp, J. L. Allen, J.-P. Jones, and M. C. Smart, *J. Electrochem. Soc.*, **165**, A361 (2018).
18. M. Weiss et al., *Adv. Energy Mater.*, **11**, 2101126 (2021).
19. N. D. Rodrigo, S. Tan, Z. Shadike, E. Hu, X.-Q. Yang, and B. L. Lucht, *J. Electrochem. Soc.*, **168**, 070527 (2021).
20. J. Kim, S. M. N. Jeghan, and G. Lee, *Microporous Mesoporous Mater.*, **305**, 110325 (2020).
21. C. Li, X. Zhang, K. Wang, X. Sun, and Y. Ma, *J. Power Sources*, **400**, 468 (2018).
22. N. Kim, S. Chae, J. Ma, M. Ko, and J. Cho, *Nat. Commun.*, **8**, 812 (2017).
23. K.-H. Chen et al., *J. Power Sources*, **471**, 228475 (2020).
24. F. Rouquerol, J. Rouquerol, and K. S. W. Sing, *Absorption by Powders and Porous Solids* (Academic, San Diego) (1999).
25. A. C. Ferrari and J. Robertson, *Phys. Rev. B*, **61**, 14095 (2000).
26. H.-M. Cho, Y. J. Park, J.-W. Yeon, and H.-C. Shin, *Electron. Mater. Lett.*, **5**, 169 (2009).
27. J. Li, L. E. Downie, L. Ma, W. Qiu, and J. R. Dahn, *J. Electrochem. Soc.*, **162**, A1401 (2015).
28. K. Märker, P. J. Reeves, C. Xu, K. J. Griffith, and C. P. Grey, *Chem. Mater.*, **31**, 2545 (2019).
29. J. P. Pender et al., *ACS Nano*, **14**, 1243 (2020).
30. D. Zhang, B. S. Haran, A. Durairajan, R. E. White, Y. Podrazhansky, and B. N. Popov, *J. Power Sources*, **91**, 122 (2000).
31. C. Usubelli, M. M. Besli, S. Kuppan, N. Jiang, M. Metzger, A. Dinia, J. Christensen, and Y. Gorlin, *J. Electrochem. Soc.*, **167**, 080514 (2020).
32. L. Jin, C. Shen, Q. Wu, A. Shellikeri, J. Zheng, C. Zhang, and J. P. Zheng, *Adv. Sci.*, **8**, 2005031 (2021).
33. L. Jin, J. Zheng, and J. P. Zheng, *J. Electrochem. Soc.*, **168**, 010532 (2020).
34. K. G. Gallagher et al., *J. Electrochem. Soc.*, **163**, A138 (2016).
35. Y. Kuang, C. Chen, D. Kirsch, and L. Hu, *Adv. Energy Mater.*, **9**, 1901457 (2019).
36. J. Billaud, F. Bouville, T. Magrini, C. Villevieille, and A. R. Studart, *Nat. Energy*, **1**, 16097 (2016).
37. J. S. Sander, R. M. Erb, L. Li, A. Gurijala, and Y.-M. Chiang, *Nat. Energy*, **1**, 16099 (2016).
38. T. M. Bond, J. C. Burns, D. A. Stevens, H. M. Dahn, and J. R. Dahn, *J. Electrochem. Soc.*, **160**, A521 (2013).
39. J. C. Burns, D. A. Stevens, and J. R. Dahn, *J. Electrochem. Soc.*, **162**, A959 (2015).
40. J. E. Harlow, S. L. Glazier, J. Li, and J. R. Dahn, *J. Electrochem. Soc.*, **165**, A3595 (2018).